

1. Results

1.1. Virtual Prototyping of Cell Signals

During the course of this thesis, numerical simulations for the microchannel have been carried out. On the one side, a simulation about the shape of a giant magneto resistance (GMR)-sensor signal of cells was performed, where the magnetic momentum was conveyed through magnetic nanoparticles (MNPs) bound to their surface. On the other side, cell aggregates have been looked at in the same manner with different angles respective to the sensor. Both simulations were then correlated to a reference dipole, with the equivalent magnetic momentum distributed in the center of mass.

Additionally, the flow and shear field inside the channel was simulated numerically for the channel cross section as well as for a particle near the walls. A force equilibrium simulation was also established in a basic manner.

Every simulation was captured in a MATLAB class “MRCyte”, which contains material parameters and constants for all simulations above.

1.1.1. Numerical investigation of immunomagnetic label density and size on quantitative magnetoresistive sensing of single cells and cell aggregates

In order to mimic a immunomagnetically labeled cell flowing over the sensor half bridge, the planar integral of the respective magnetic flux density (\mathbf{B}) was solved analytically. Here, \mathbf{r}_i specifies the distance vector of a single MNP from the sensor plane. The magnetic flux density was converted by the GMR to a resistive change \mathbf{R}_{sig} by scaling it with the GMR-sensitivity S and subsequently into a signal voltage \mathbf{V}_{sig} inside the bridge branch.(Eqs. 1.1 to 1.3)

In the numerical approach, MNPs were randomly sampled on a sphere surface with an equivalent diameter of 4 μm or 8 μm . Then, the signal was computed for every MNP during every timestep. Additionally, the MNP distribution was rotated in every iteration to resemble a rolling motion. The computed signals were then cross-correlated to the signal of a reference flux density \mathbf{B}_{ref} caused by a point-like magnetic moment located in the geometric center of the same sphere.

$$\mathbf{B}(t) = \sum_{i=1}^N \frac{1}{A_{\text{Sensor}}} \int_{-\frac{l}{2}}^{\frac{l}{2}} \int_{-\frac{w}{2}}^{\frac{w}{2}} \frac{\mu_o}{4\pi} \left(\frac{3\mathbf{r}_i(t) (\mathbf{r}_i(t) * \mathbf{m}_i)}{|\mathbf{r}_i(t)|^5} - \frac{\mathbf{m}_i}{|\mathbf{r}_i(t)|^3} \right) dx dy \quad 1.1$$

$$\mathbf{R}_{sig}(t) = -\mathbf{B}(t) * \frac{S}{100} * R + R \quad 1.2$$

$$\mathbf{V}_{sig}(t) = \frac{\mathbf{R}_{sig}(t)}{R + \mathbf{R}_{sig}(t)} * V_p - \frac{V_p}{2} \quad 1.3$$

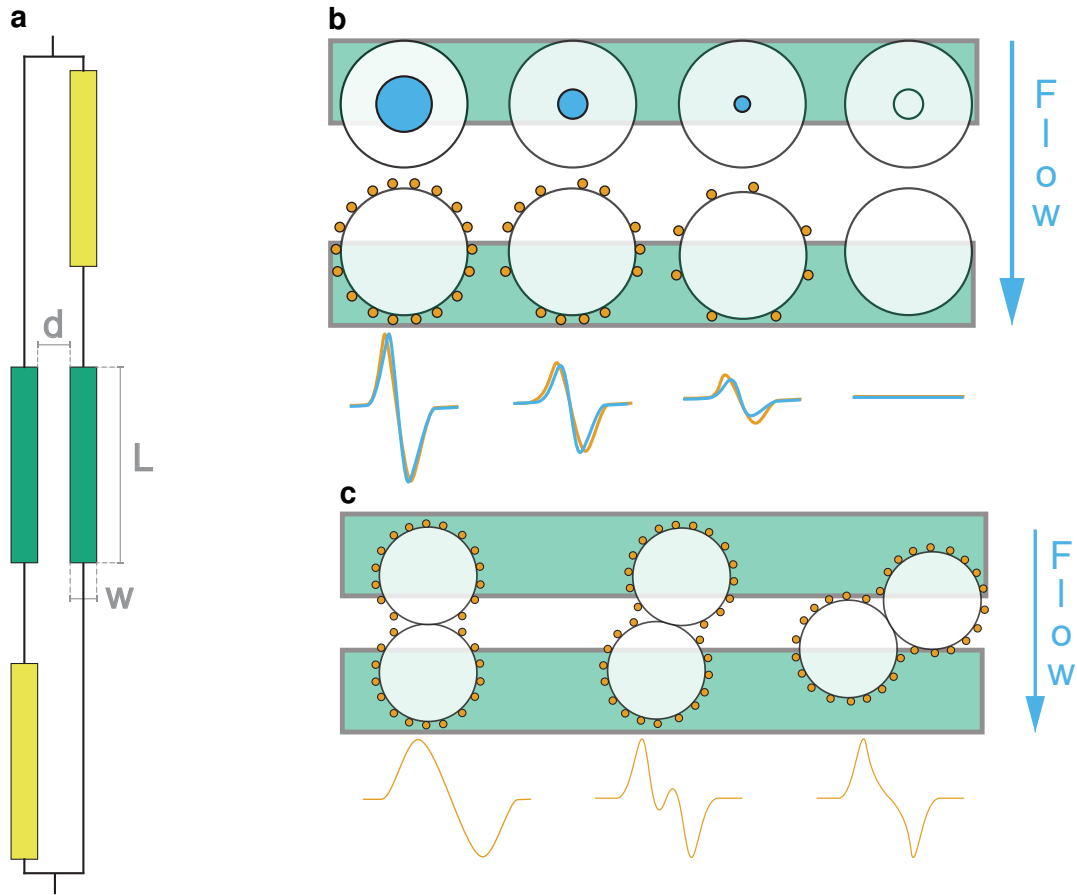


Figure 1: Particle Coverage Simulation

(a) Dimensions of the GMR Wheatstone bridge sensor: Distance d between both variable bridges (green), width w of a GMR-sensor, length L of a sensor. (b) Scheme of single cell simulation: The ideal magnetic dipole in the geometric center of a sphere (●) causes a signal deviation from the real cell signal with magnetic moment distributed on the cell surface. (c) Signal shapes of different angles of two-particle aggregates lead to differing signal shapes.

By its formula, cross-correlation $R_{xy}(\tau)$ yields a displacement dependent signal through its convolution of the complex conjugated reference signal $V_{ref}^*(t)$ with the sample signal $V_{sig}(t + \tau)$. (Eq. 1.4) Therefore, only the maximal correlation of this function was considered in further analyses.

$$\max\{R_{xy}(\tau)\} = \max\left\{\int_{-\infty}^{\infty} V_{ref}^*(t) V_{sig}(t + \tau) dt\right\} \quad 1.4$$

Signal Similarity
for Cells With
varying Bead
coverages, Cross-
correlation
between single
pole with
magnetic
moment and
surface covered
with randomly
distributed mag-
netic particles,
simulation of cell
sliding velocity
and force

Parameter	Unit	Value	Explanation
w	m	2.0×10^{-6}	GMR width
l	m	30.0×10^{-6}	GMR length
d	m	14.0×10^{-6}	Distance between two sensors
R	Ω	250	GMR Resistance
V_p	mV	100	Supply voltage
$t_{free\ layer}$	m	7.0×10^{-9}	Thickness of free layer
M	$A\ m^{-1}$	2.0×10^4	Volume Magnetization
$V_{noise,rms}$	V	2.5×10^{-6}	Artificial noise
Sim. Space	m	$[-25 \times 10^{-6}, 25 \times 10^{-6}]$	Interval around sensor center

Table 1: Magnetic Simulation Parameters

Constants used inside the framework for the simulation of the magnetic field inside the GMR Wheatstone half bridge. The volume magnetization was adapted according to the simulated particle size.

1.1.2. Single Cell Signal

Aim of these simulations is to find a measure of how magnetic labeling of a cell affects signal shape and its subsequent analysis. A single cell with a surface coverage of 5 % to 99 % of a densely packed sphere was loaded randomly with MNPs at different sizes. Then, the previously explained rolling motion over the sensor bridge was simulated with the parameters specified in Table 1. After correlation of the resulting signal voltage to the reference dipole signal (Fig. 1b, ●) with three randomly MNP distributions, the dependency on the coverage was evaluated. As shown in the schematic Fig. 1b, an increase in signal peak amplitude but also in full width at half maximum (FWHM) at growing coverage was expected .

The expected behavior matches the data analysis (Fig. 2). Each two analyzed sphere diameters $4\ \mu m$ and $8\ \mu m$ with MNP sizes ranging from 20 nm to $2\ \mu m$, show a great standard error of the mean (SEM) at low coverage. This very probably is subjected to the momenta of single particles which play a greater individual role and hence influence the signal shape significantly because the overall dipole momentum in the sensor loses homogeneity.

Another observable effect is related to the MNP size. Absolute correlation differs from 20 nm to the ten and hundred fold diameter significantly. This can be related to the magnetic momentum per MNP as it is dependent on the volume - thus r^3 . However, for bigger magnetic particles this does not hold true because the composition changes from pure magnetite to a polymer shell with embedded oxide core at around 150 nm.

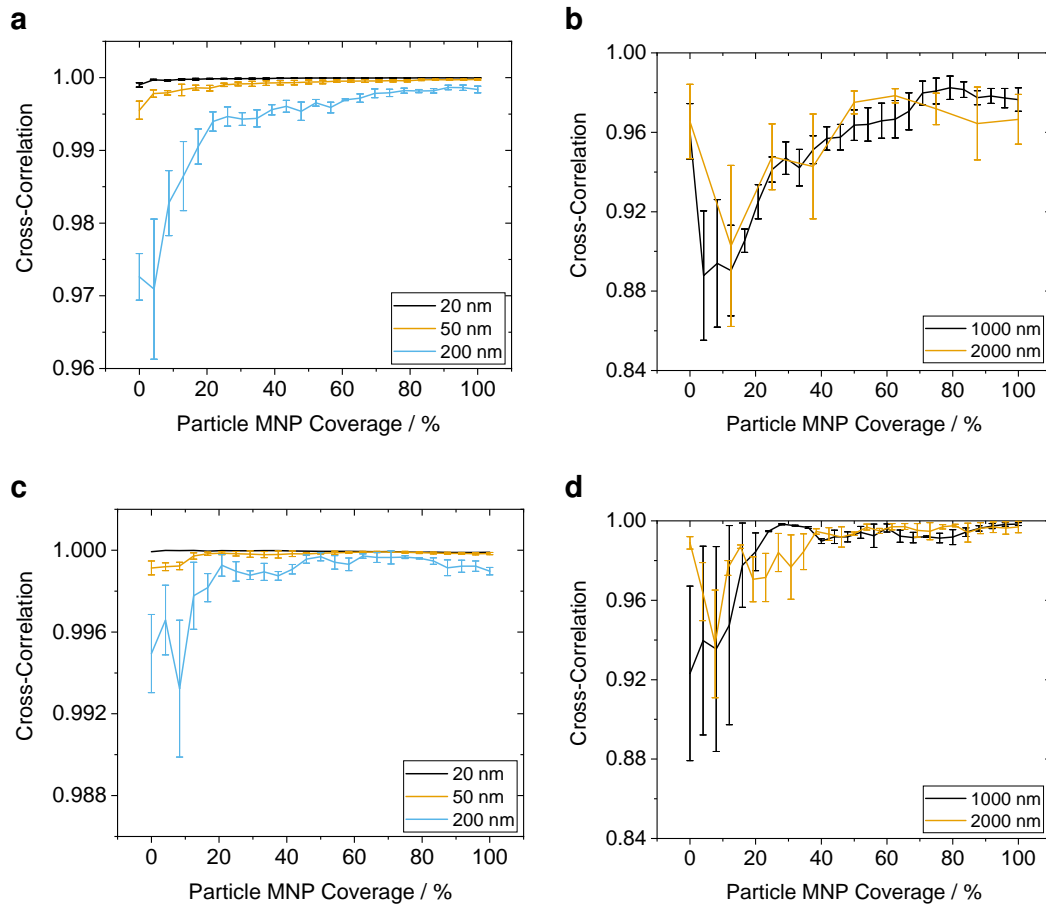


Figure 2: Coverage Dependent Signal Correlation

MNP coverage of a sphere with 4 μm (a, b) and 8 μm diameter (c, d) covered by magnetic particles ranging from 20 nm to 2000 nm. A cross-correlation increase which is inversely proportional to the MNP size can be observed.

Nevertheless, larger particles carry also greater magnetic momentum which brings also the aforementioned influence of single MNPs into consideration for that effect.

Also, the densely packed sphere surface can evidently carry more smaller than larger MNPs. This ranges from 641 600 MNP at 20 nm to 81 at 2 μm for a sphere radius of 4 μm and limits the maximum achievable momentum.

In reality, a maximum immunomagnetic label density depends not on the densely packed sphere but rather on the present antigens, and association or dissociation constants. Therefore, a complete saturation coverage is not achievable under physiological conditions. This leads to the fact that any possible momentum by deposition of 20 nm and 50 nm on a cell surface cannot be resolved from noise by this sensing setup.

Also, it can be seen that the correlation approaches a maximum obtainable value for every MNP size. Referenced for both simulated sphere diameters in (Fig. 3a), an inverse proportionality between correlation and MNP diameter is visible. The trend in respective maxima can be related to differences in the magnetic momentum amplitude and coverage inhomogeneity.

Inter-sphere compared, maximum correlation shows also a significant decrease in for

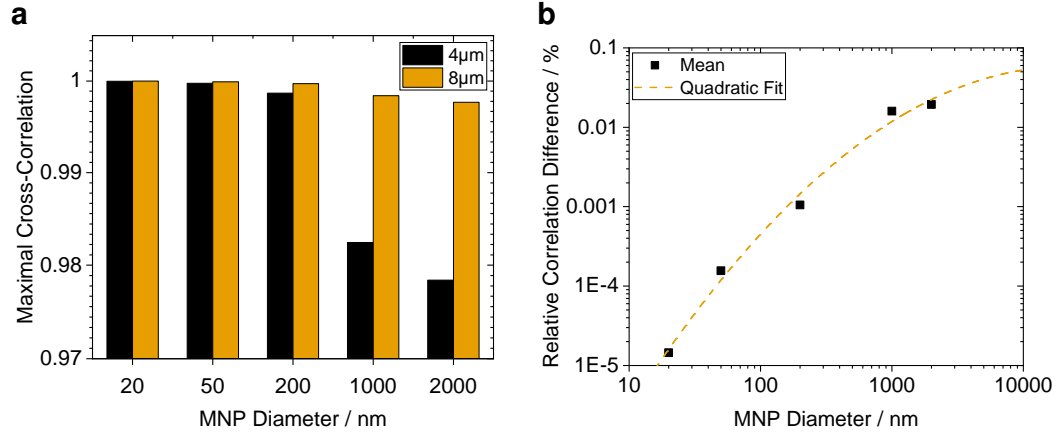


Figure 3: Maximal Cross-Correlation Differences

(a) Mean coverage at 99 % for 4 μm and 8 μm spheres. A negative dependency on the MNP size can be explained by the ratio of magnetic momentum per unit surface and its homogeneous distribution across the whole surface.
(b) Relative correlation error between 4 μm and 8 μm spheres with a quadratic fit. The quadratic behavior could be related to the relative surface area which can be occupied by magnetic momentum. (Adj. $R^2 = 0.992\ 09$)

higher MNP sizes as the particle diameter itself increases. The relative error between both sizes - as computed in Eq. 1.5 - is depicted in Fig. 3b. Assuming a dependency on the available particle surface and subsequently the fraction which can be occupied by MNPs, a quadratic fit seems appropriate. (Eq. 1.6) The fit could indicate that a reference dipole cannot be discriminated from a cell at small MNP diameters while the correlation error becomes nearly constant at great MNPs.

$$\text{Relative Correlation Difference} = 1 - \frac{\max\{\text{Cross-Correlation}(d = 4\ \mu\text{m})\}}{\max\{\text{Cross-Correlation}(d = 8\ \mu\text{m})\}} \quad 1.5$$

$$\text{Relative Correlation Difference} = -0.385\ 32\ d_{MNP}^2 + 3.345\ 74\ d_{MNP} - 8.496\ 29 \quad 1.6$$

1.1.3. Cell Aggregates

In another simulation, two 200 nm-MNP-covered spheres were attached to each other in differing angles and simulated flowing over the sensor. Signal similarity to a magnetic dipole in the center of a single reference sphere was computed by cross-correlation. As can be observed in Fig. 4, correlation is identical to a single sphere at low coverages when the magnetic momentum is high enough to form a uniform magnetic field. At occupancies greater than 50 %, the two attached cells have to be considered as individual dipoles in superposition and thus show a signal that carries small peaks in the center. This is shown schematically in Fig. 1c. In term, this causes a high signal deviation from the reference and thus a low degree of correlation.

FlowField Simulations!!!!

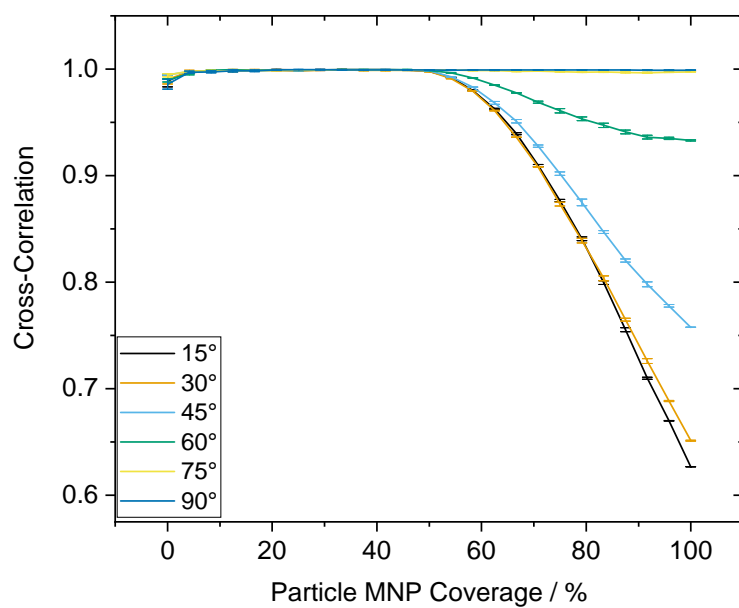


Figure 4: Signal Correlation between Two-Cell Aggregates At Shifting Angles

Two-Sphere aggregates are covered with 200 nm MNPs and simulated flowing over the sensor at differing respective angles. The SEM indicates a difference in cross-correlation of three truly random MNP distributions. For low yaw angles and high coverages, the aggregate's signal reflects rather two single dipoles in superposition than one quite homogeneous dipole. This causes a high signal deviation from the reference and thus a low degree of correlation.

1.2. Reference Bead Surface Functionalization

After simulation of the coverages, biotin was titrated on 8 μm reference beads with two different surface terminations in order to selectively bind MNPs with the counter-agent streptavidin to the surface. First, $-\text{NH}_2$ (amine)-microbeads were modified by sulfo-NHS-biotin. Second, $-\text{COOH}$ (carboxyl)-beads were coated by amine-PEG₂-biotin via EDC-NHS-activation. On the same beads Anti-IgG1-PE antibodies were titrated after the same coupling chemistry.

Subsequently, biotin-coated beads were analyzed in the flow cytometer in the by staining with Atto-488 (Ex: 500 nm, Em: 520 nm) coupled streptavidin. The antibody was already industrially modified with phycoerythrin (PE) and measured at 488 nm excitation and 585 nm emission wavelength. The gating was standardized by the strategy found in ??, ??. Subsequently, the median fluorescence intensity (MFI) was computed and fitted with a Hill-function.(??) Stability of carboxylated and aminated beads and subsequently their respective modification protocols was evaluated for 12 days.

1.2.1. Amine-Surface Biotinylation

As first approach, polystyrene copolymer microbeads with 8 μm diameter were functionalized by (sulfo-)NHS-biotin after a standard protocol. A titration of the biotin reactant yielded a varying surface coverage as shown in Fig. 6a. During this one-pot-reaction, the water-soluble sulfo-NHS-biotin forms an $\text{R}_1-\text{CONH}-\text{R}_2$ (carboxamide) linkage with the primary amine and 1-hydroxy-2,5-dioxopyrrolidine-3-sulfonate splits off as byproduct.

As can be seen from the SEM error-bars from the plot 6a, which were constructed from three true biological replicates, this process is highly reproducible. Therefore, an surface coverage in different grades of biotinylation could be obtained accurately with a high confidence level.

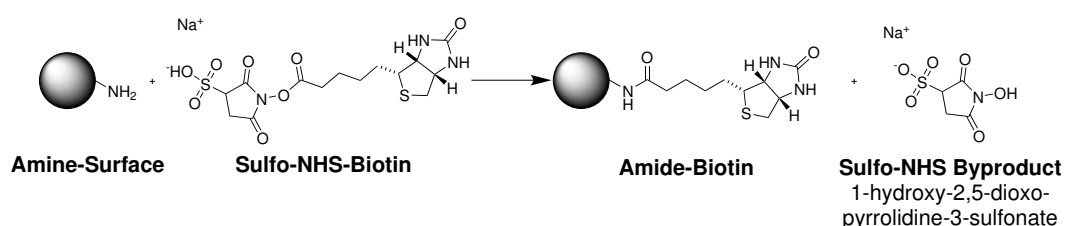


Figure 5: Amine Bead Modification with Sulfo-NHS-Biotin

An amine terminated bead brought into reaction with sulfo-NHS-biotin. Both form an amide linkage and bind biotin covalently to the surface. As byproduct the sulfo-NHS-ester splits off.

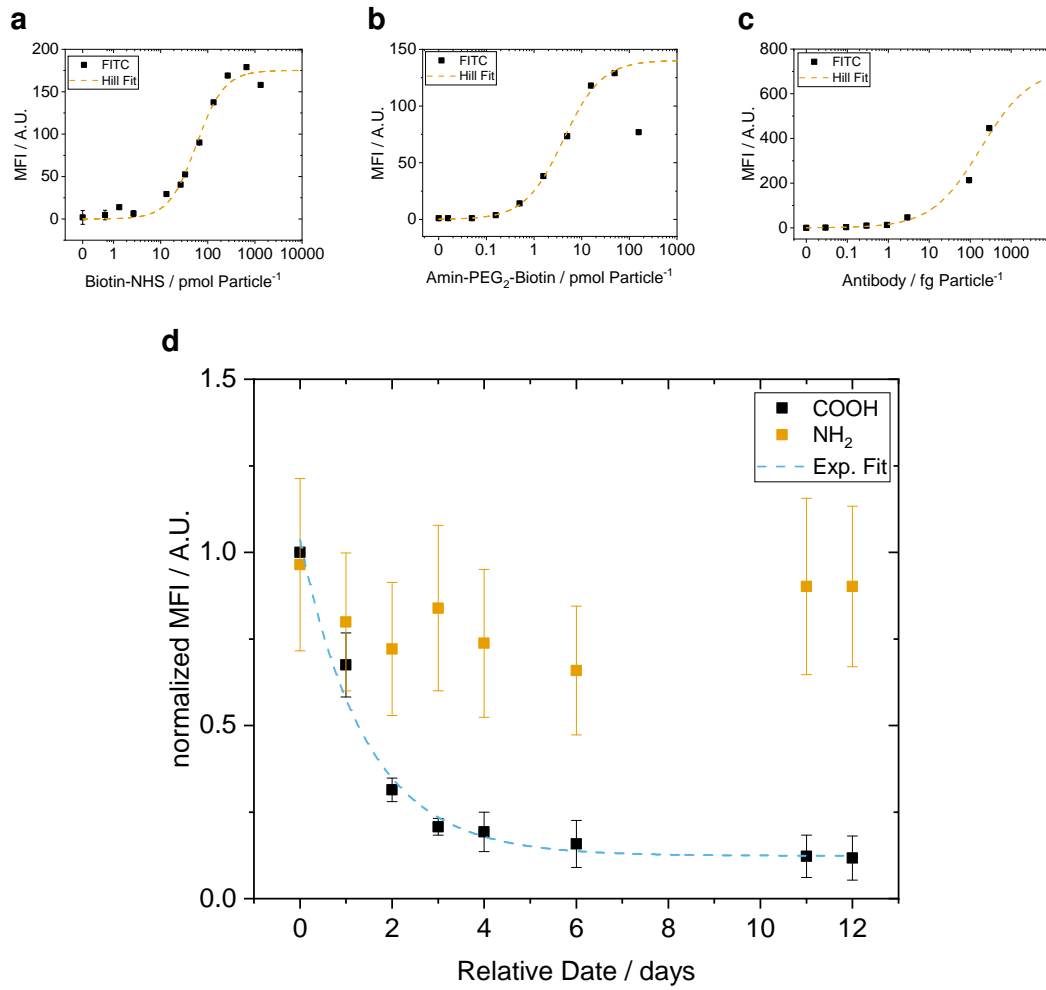


Figure 6: Titration of Biofunctional Molecules on 8 μm Particles

Titration curves of NHS-biotin (a), Amin-PEG₂-Biotin (b), and Anti-IgG1 (c) with their respective Hill fits. The corresponding fit parameters as well as the goodness factor are shown in Table 2a. (d) Stability analysis of functionalized carboxyl and amine beads over 12 days. The carboxylate particles show a exponential decrease with a half-life of 1.43 days as determined by the exponential fit. The respective parameters are shown in Table 2b.

a

Param.	Hill 6a	Hill 6b	Hill 6c
V_{max}	175.216 19	140.391 53	713.836 43
k	57.367 13	4.126 61	182.830 11
n	1.474 88	1.074 93	0.724 58
Adj. R^2	0.981 21	0.997 22	0.992 26

b

Param.	Exp. 6d
A	0.912 63
τ_{decay}	1.425 57
y_0	0.123 69
Adj. R^2	0.966 55

Table 2: Fit Parameters of Biotinylation

(a) Coefficients for the Hill fits in Figs. 6a to 6c (b) Exponential fit coefficients for the stability analysis in Fig. 6d

Carboxylate-Surface Biotinylation

Biotin-amin protocol

stabilität

antikörper

1.3. Concentration Measurements in MRCyte

Driving factor for the concentration measurement is the absolute count of immunomagnetically labeled cells in whole blood or at least diluted whole blood which is not possible in today's optics-based devices mostly due to red blood cells (RBCs). Therefore, with the in ?? described sensor setup, absolute concentrations of magnetic reference beads were attempted to measure.

Consequently, beads with acrylate surface were pumped through a microfluidic channel with a permanent underneath. The magnet drew every magnetic particle to the ground, where they were focused on the sensor bridge and subsequently measured there. From the received signal several parameters such as peak amplitudes, locations, zero-crossings, and relative distances between each other were computed. (Fig. 7) However, for a concentration measurement mostly the correct detection of a signal from the noisy stream or from a superposition of multiple simultaneously measured particles was critical. The related error sources and countermeasures will be elaborated in Section 1.3.1.

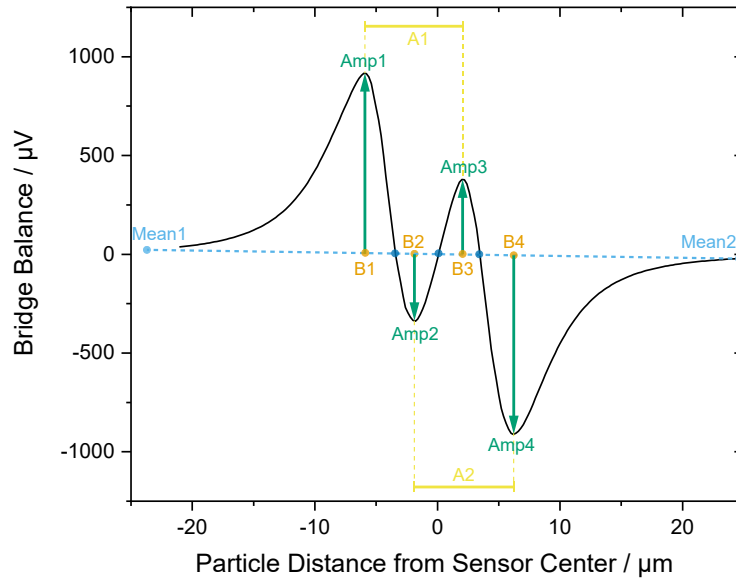


Figure 7: Example Signal of Magnetic Measurement

Signals generated from the Wheatstone bridge sensor setup feature a certain shape which allows for several measures. In case the overall signal stream carries a constant or linear offset, it is scaled to the means before and after the detected peak pattern. (Mean1, Mean2) The x- and y-Positions of each peak are denominated by B1-4 and Amp1-4, respectively. The crossings of the signal through the linear connection of both means are denominated by B1-3 (in the figure by ●). Further, the difference between the equally oriented peaks B3-B1 and B4-B2 give a measure for the homogeneous movement of the measured object and are called A1 and A2 each. From these values the overall velocity can be approximated because the GMR distance and sample rate is fixed precisely. Analogously, the magnetic diameter of a dipole is computed by the mean of the differences B2-B1 and B4-B3.

By measuring the absolute concentration with a commercially available device, the flow cytometer (MacsQuant 10, Miltenyi), a reference bead count was established. In a pre-test, beads were taken directly from the microcentrifuge tube, after pumping through a syringe and after pumping through a syringe with 10 cm of connected through tubing (ID 0.5 mm, RS Chemicals). Afterwards, they were counted in the flow cytometer in equal volumes. Additionally, two different buffers - MACS running buffer (MACS) and phosphate buffered saline (PBS) - and two different surface terminations were used. Both buffers are based on phosphate buffered saline (PBS). Notwithstanding MACS contains 2,2',2'',2'''-(Ethane-1,2-diylidinitrilo)tetraacetic acid (EDTA) as chelator for divalent ions, Tween 20 - a non-ionic surfactant -, and an azide-based stabilizer. Hence, the wetting of surfaces and the electrostatic interactions of these buffers differ. The same properties were varied on the bead surface by choosing acrylate and biotin terminated beads.

In Fig. 8, a trend (without statistical confidence) can be observed that shows a decrease in particle counts after every additional surface which beads could potentially interact with. In term, a correct count in absolute numbers seems out of range. However, a calibration of the system with the flow profile inside the channel to compensate for losses subjected to connectors and magnetic enrichment structures was carried out successfully.

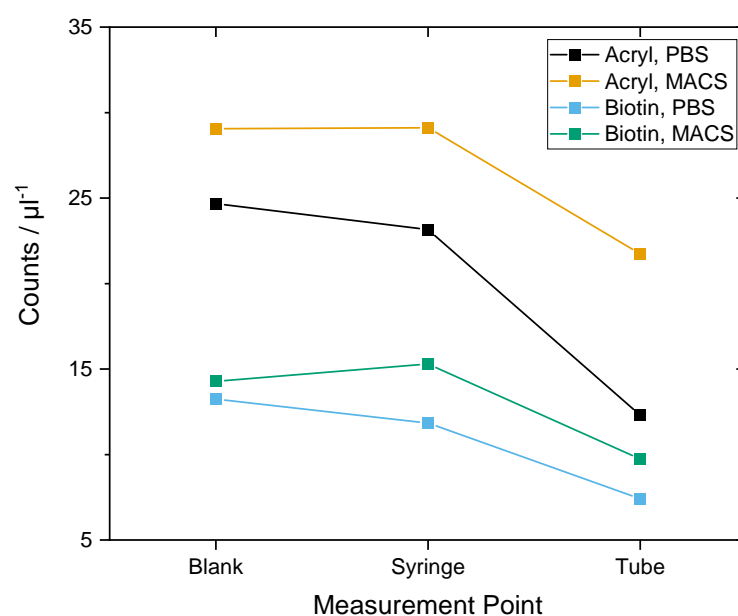


Figure 8: Bead Loss Evaluation in Connectors

Bead concentrations measured in equal volumes in the flow cytometer after being pumped through a syringe or a syringe with connected tubing. The blank sample was measured directly from the stock solution. Additionally, electrostatic and surface tension related effects were resolved by the usage of different buffers and bead surfaces.

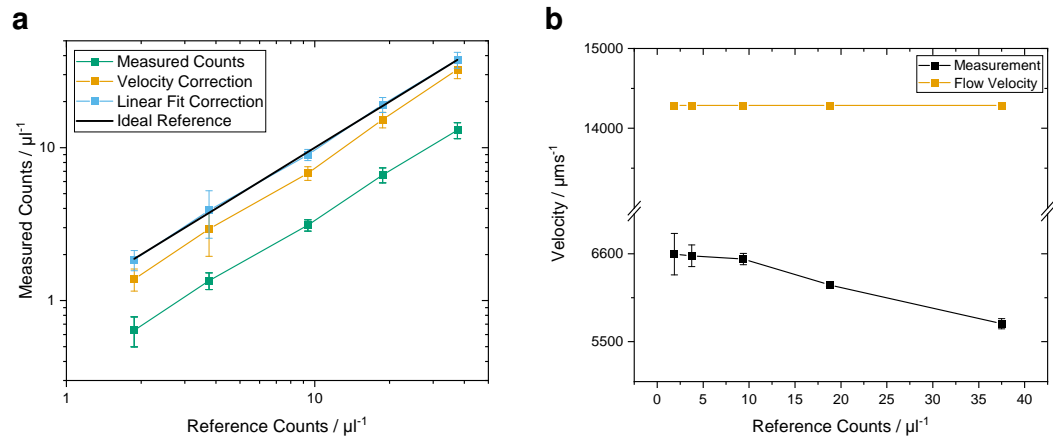


Figure 9: Absolute Concentration Measurements

Mean from 3 independent measurements (a) mean, sd (b) mean, SEM, Reference Count based error: Linear fit steepness $0.34622 \pm 0.00968 \rightarrow$ Correction Factor (inverse) 2.88833 ± 0.08075 , Velocity Based Correction: Q/A Dims: $700 \mu\text{m} \times 50 \mu\text{m}$ $Q = 30 \mu\text{L min}^{-1} \rightarrow 2.26109$

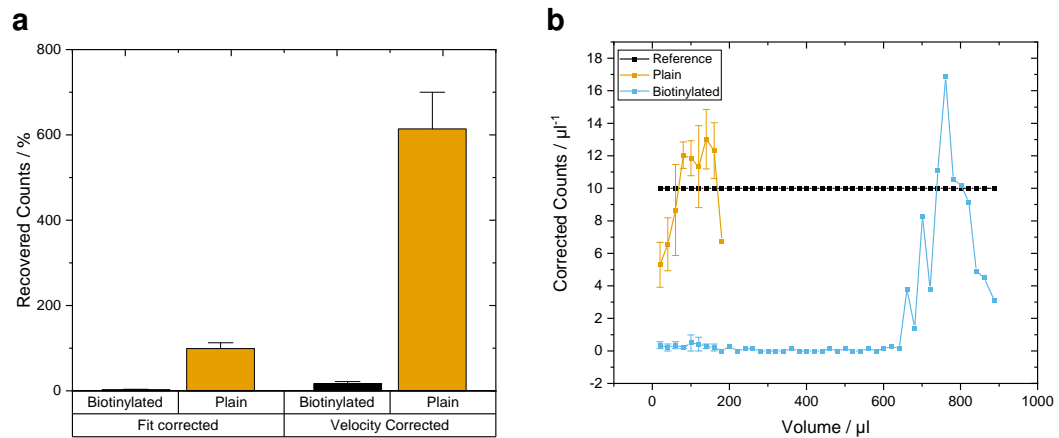


Figure 10: Error Sources in Concentration Measurements

(a) mean, SEM Fit factor comparison with protein coated surfaces (b) mean, SEM

1.3.1. Calibration of Flow Field

Velocity Correction factor Linear Approximation correction factor

1.3.2. Count Stability

Measurement over 1h

Concentration Measurement in Diluted Whole Blood

1.3.3. Differential Counting Setup

Sensitivity Calibration

Concentration Measurement in Buffer Solution

1.3.4. Surface Magnetization of Biofunctionalized Beads

Somehow BNF-Dextran showed unspecificity initially, but not anymore later on

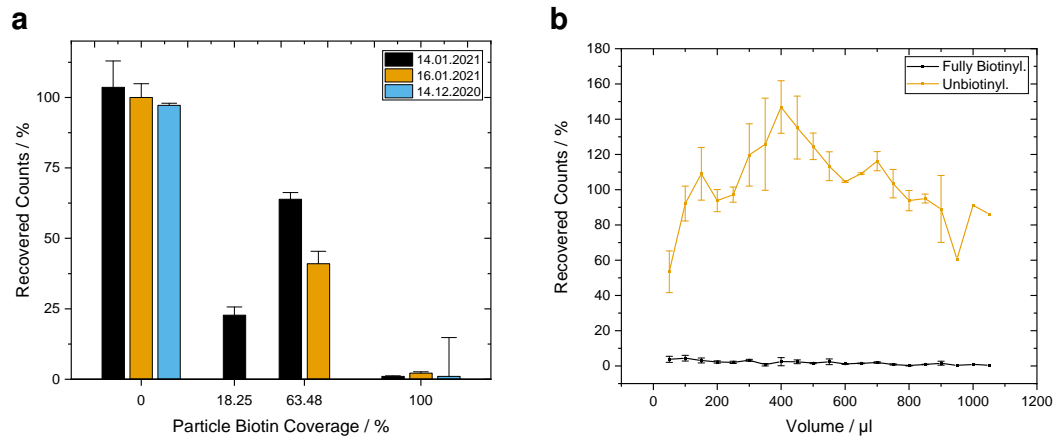


Figure 11: Reproducibility of Concentration Measurements with Saturated Neutravidin Surface
 (a) $80 \mu\text{L min}^{-1}$ mean, SEM (b) All, mean, SEM,

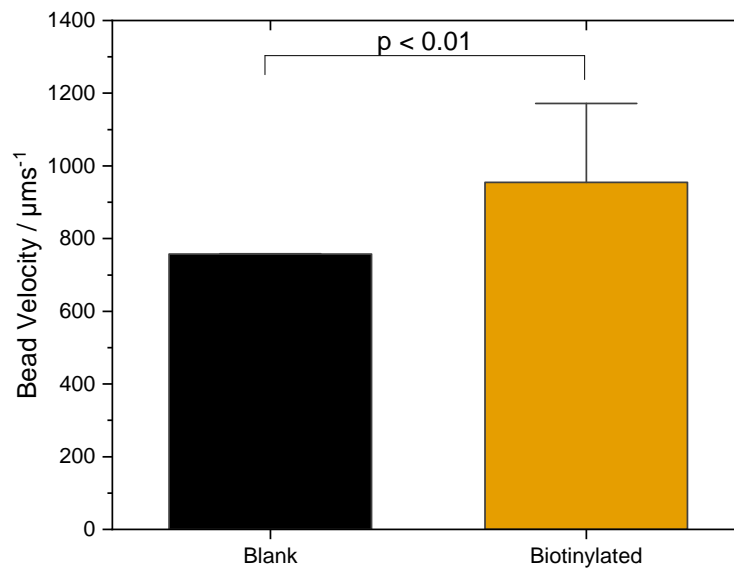


Figure 12: Measured Bead Velocity
 $p < 0.01$

1.4. Surface Modification and Biofunctionalization of the Sensor Chip Substrate

1.4.1. Physisorption

Quantification in Plate Reader Trial with Neutravidin + Sensor (Esthis Versuch)

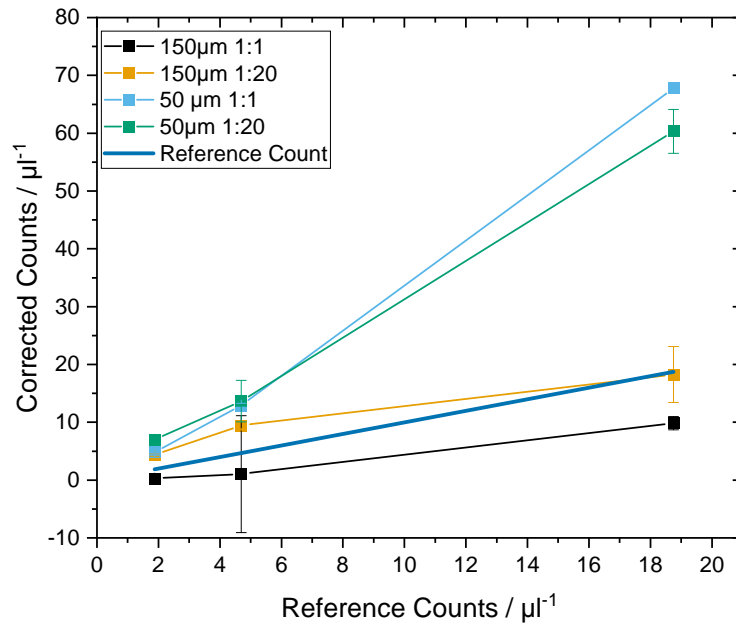


Figure 13: Absolute Concentration Measurement in Blood Samples Under Varying Channel Height
Velocity Correction does not work for high concentrations in 50 μm

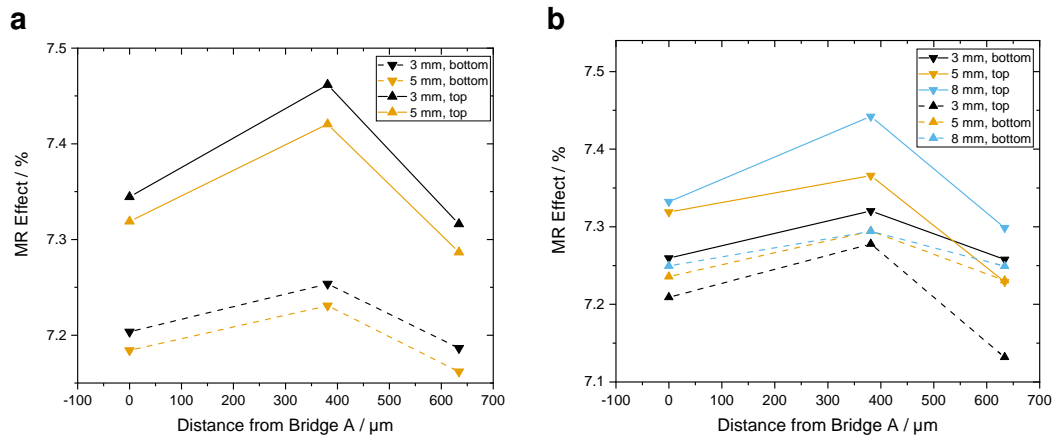


Figure 14: Hysteresis Calibration for Stacked Printed circuit board (PCB)
(a) Optimized for top sensor (b) Optimized for bottom sensor

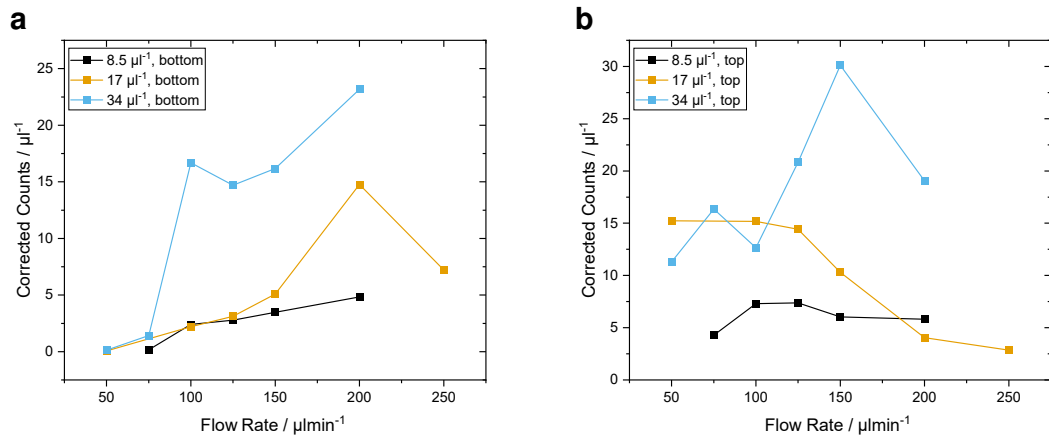


Figure 15: Flow Rate Dependency of Counting Setup
(a) Optimized for top sensor (b) Optimized for bottom sensor

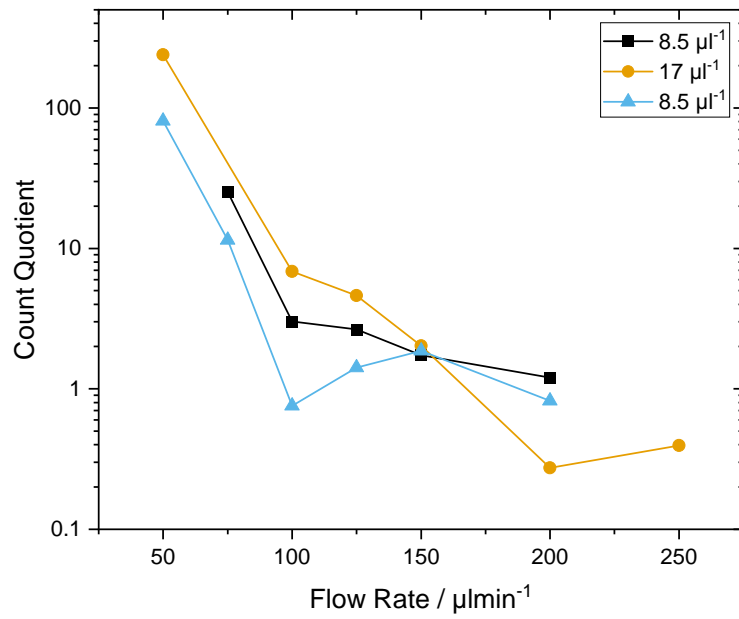


Figure 16: Optimal Differential Counting Flow Rate
Losses in different buffers and bead surfaces.

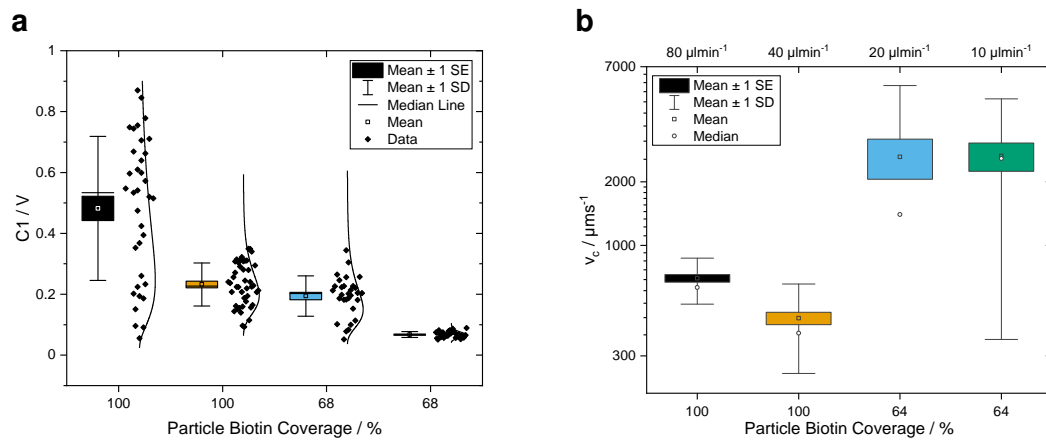


Figure 17: Bead Coverage Assay with BNF-Dextran-redF-100 nm
(a) 1. 80 $\mu\text{L min}^{-1}$ 2. 40 $\mu\text{L min}^{-1}$ 3. 20 $\mu\text{L min}^{-1}$ 4. 10 $\mu\text{L min}^{-1}$ (b) $d = 8 \mu\text{m}$

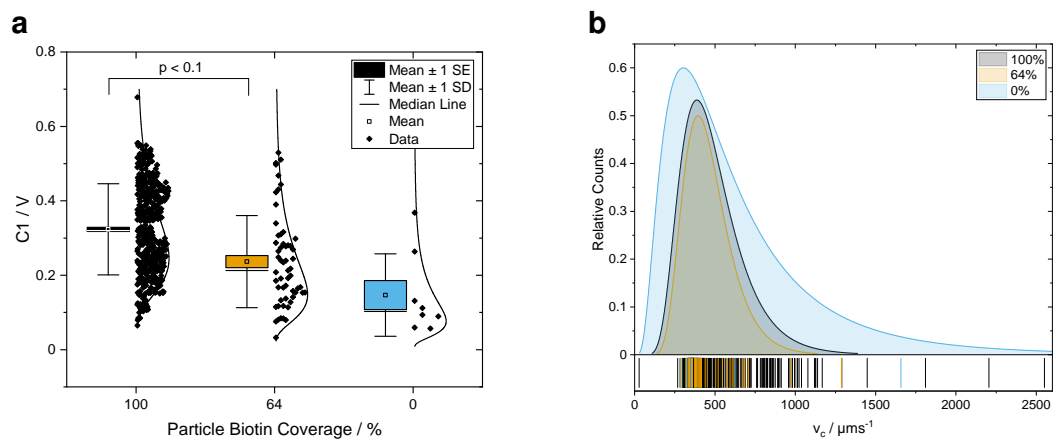


Figure 18: Bead Coverage Assay with OceanNanotec 50 nm
Mean from 3 different particle distributions at maximum coverage, SEM (a) $d = 4 \mu\text{m}$ (b) $d = 8 \mu\text{m}$

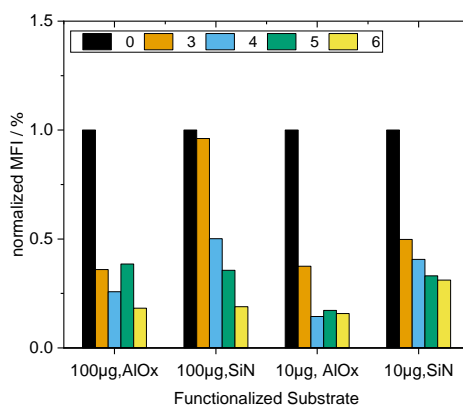


Figure 19: Surface Adsorption Stability of Neutravidin on Silicon nitride (Si_3N_4) and Aluminium oxide (Al_2O_3)
Blank with PBS and Blank substrate, corrected, then normalized, absolute protein per ~25 mm

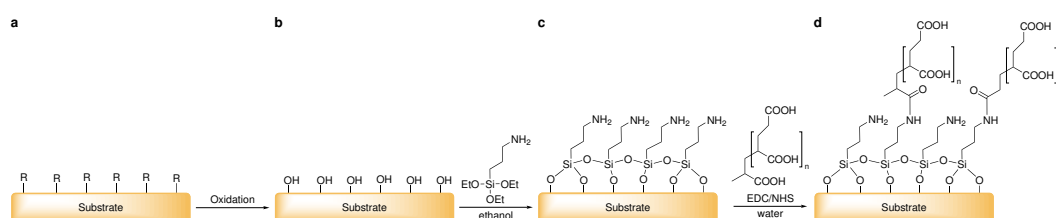


Figure 20: General process chain of chemical surface modification

Any substrate with various surface groups R (a) is oxidized to exhibit $-\text{OH}$ (hydroxyl) groups.(b). Then a silane self-assembled monolayer (SAM) is attached (c) and subsequently modified by carbodiimide chemistry with Poly(acrylic) Acid (PAA). (d)

1.4.2. Covalent Attachment

Plasma-Based Approach

Water-Based Approach

Sonicate in Acetone and Water 5' 1:1 hydrochloric acid (HCl):Methanol sulfuric acid (H_2SO_4) Treat for 30 min in light boiling water

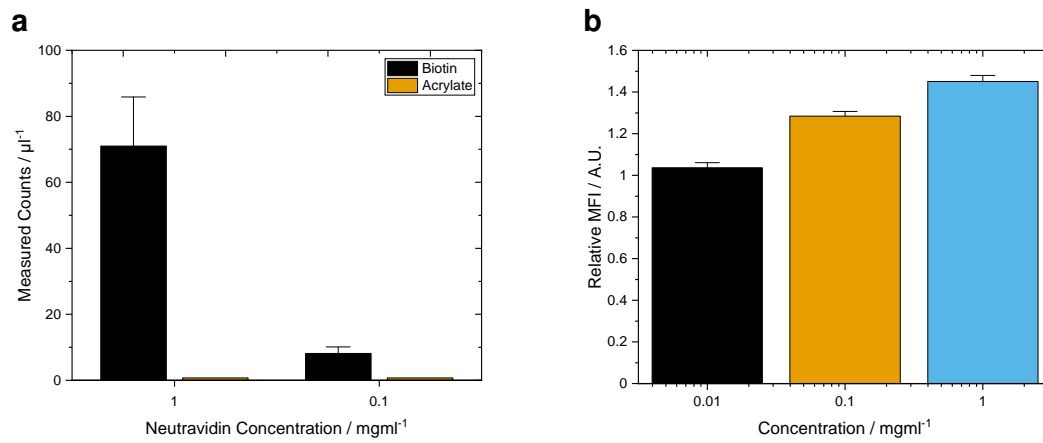


Figure 21: Neutravidin Titration Fluorescence and Bead Capture Assay
 Relate count to area, then change MFI to counts $\mu\text{L}^{-1} \text{mm}^{-2}$ (a) Serpentine (b) Glass

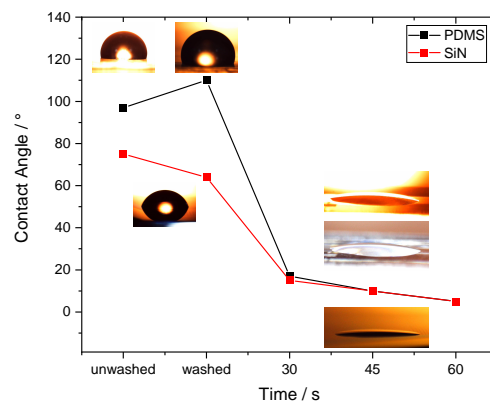


Figure 22: Hydrophobicity Analysis of poly(dimethyl siloxane) (PDMS) under Plasma Exposure
 test123